JGR Space Physics

RESEARCH ARTICLE
10.1029/2018JA026225

SuperDARN Evidence for Convection-Driven Lagrangian Coherent Structures in the Polar Ionosphere

U. Ramirez[1], Ningchao Wang[1], Alex T. Chartier[2], and S. Datta-Barua[1]

[1]Mechanical, Materials, and Aerospace Engineering, Illinois Institute of Technology, Chicago, IL, USA, [2]Johns Hopkins University Applied Physics Laboratory, Laurel, MD, USA

Key Points:
- Lagrangian coherent structures (LCSs) exist in Super Dual Auroral Radar Network (SuperDARN) ionospheric plasma flows
- A two-cell convection pattern results in a W-shaped LCS, but when the two-cell pattern breaks down the LCS loses its shape
- Analysis of two polar cap patches shows that the center of each patch originated from plasma on the main LCS ridge

Supporting Information:
- Supporting Information S1
- Movie S1
- Movie S2
- Movie S3

Correspondence to:
U. Ramirez,
uramirez@hawk.iit.edu

Citation:
Ramirez, U., Wang, N., Chartier, A. T., & Datta-Barua, S. (2019). SuperDARN evidence for convection-driven Lagrangian coherent structures in the polar ionosphere. *Journal of Geophysical Research: Space Physics*, *124*, 3573–3588. https://doi.org/10.1029/2018JA026225

Received 22 OCT 2018
Accepted 19 MAR 2019
Accepted article online 1 APR 2019
Published online 13 MAY 2019

©2019. American Geophysical Union. All Rights Reserved.

Abstract Polar cap patches are large sporadic enhancements of plasma density on the scale of hundreds of kilometers, which can impact the performance of Global Navigation Satellite Systems. Lagrangian Coherent Structures (LCSs) are ridges that show areas of maximal separation in a time-evolving flow. Previous work based on modeled ionospheric flow showed that LCSs exist in the ionosphere and are barriers governing patch formation. In this work, we identify the first data-driven LCSs in the high-latitude ionosphere using Super Dual Auroral Radar Network (SuperDARN) ion convection fields. The LCSs found using the Ionosphere-Thermosphere Algorithm for LCSs are compared during geomagnetically quiet and active periods. The shape of the LCS is found to be dependent on the electric potential pattern. A consistent two-cell pattern results in a W-shaped LCS, but when the two-cell pattern breaks down, the LCS loses this characteristic shape. The changes in the electric potential, and thus the LCS, are likely due to changes in the interplanetary magnetic field. A comparison between LCSs obtained from empirical models and data reveal that the data-driven LCSs are poleward of and have a shorter longitudinal span than the model-based LCSs. A comparison of the LCS location and the formation of a polar cap patch on 17 March 2015 showed that the center of the patch developed from plasma on the main LCS ridge, and this is confirmed with a separate polar cap patch event from 26 September 2011.

1. Introduction

Polar cap patches are large sporadic enhancements of the *F* layer ionosphere at high latitudes on the scale of hundreds of kilometers (Carlson, 2012; Crowley, 1996). Polar cap patches are known to lead to scintillation, which is a rapid fluctuation in the signal amplitude or phase of radio waves (Yeh & Liu, 1982). Scintillation happens as a result of the scattering of the electromagnetic waves due to changes in electron density (Sotnikov et al., 2014). Scintillation can degrade the performance of the Global Navigation Satellite System (GNSS) by causing loss of satellite lock and may lead to positioning errors (Moen et al., 2013; Pi et al., 2017). Previous work has proposed that polar cap patches may lead to scintillation through one or more of the following instability mechanisms: gradient drift, current convective, and Kelvin-Helmholtz instabilities, as well as small-scale "turbulence" processes (Atul et al., 2018; Burston et al., 2016; Moen et al., 2013). Because of this, it is important to study the formation and propagation of polar cap patches.

Zhang et al. (2013) classified polar cap patches as follows: Type L (low density), for those produced by particle precipitation; and Type H (high density), for those that originate from the segmentation of a tongue of ionization. In this paper, we focus on Type H patches. There have been many proposed mechanisms explaining the formation of polar cap patches. The typical mechanism suggests that they are formed when the boundary between the open and closed field lines (OCB) moves equatorward to a region with high-density plasma followed by the boundary relaxing, moving poleward, and carrying with it the high-density plasma (Carlson et al., 2006; Lockwood & Carlson, 1992; Lockwood et al., 2000). In addition, it has been proposed that polar cap patches form after the disruption of the ionospheric convection pattern caused by changes in the interplanetary magnetic field (IMF) (Anderson et al., 1988; Rodger et al., 1994). Bust and Crowley (2007) found that they form from plasma in the morning and evening cells around 62° geographic latitude.

In general, plasma motion has components parallel and perpendicular to the local magnetic field. The motion is the sum of the electric Pedersen drift, gravitational Pedersen drift, pure gravitation drift, and parallel mean flow (Atul et al., 2018; Sotnikov et al., 2014). Specifically, in the high-latitude ionosphere, plasma motion is coupled to the magnetosphere and the IMF. The magnetic field lines circulate over the poles from

the day to night sectors with return flow around the dusk and dawn sides due to interaction with the solar wind (Hunsucker & Hargreaves, 2003). This circulation usually forms a two-cell electric potential pattern (Hunsucker & Hargreaves, 2003) which, when combined with Earth's magnetic field, causes the plasma to drift in the $\vec{E} \times \vec{B}$ direction (Tascione, 2012).

After patch formation the patches propagate with this $\vec{E} \times \vec{B}$ motion. The typical scenario states that $\vec{E} \times \vec{B}$ drift dominates such that patches are propagated from day to night along the pathlines of the two-cell convection pattern (Carlson, 2012; Lockwood & Carlson, 1992; Moen et al., 2006; Zhang et al., 2015, 2011, 2013). Alternately, Zhang et al. (2016) found a scenario in which a stirred lobe cell in the dusk sector, due to IMF changes, prevented its propagation across the polar cap.

Polar cap patches may be sensed by single-instrument in situ measurements of density such as those from the Defense Meteorological Satellite Program (DMSP) (Greenspan et al., 1986). However, ionospheric imaging of patch density gives a synoptic view of high-latitude plasma. As discussed in the work of Bust and Mitchell (2008), plasma density is estimated based on direct electron density measurements and on path-integrated total electron content (TEC) measurements from multiple instruments, combined. One such algorithm is Multi-Instrument Data Analysis System (MIDAS) (Chartier et al., 2012; Mitchell & Spencer, 2003; Spencer & Mitchell, 2007).

Recently, the relationship between a polar cap patch imaged with MIDAS and a type of fluid coherent structure was investigated (Wang et al., 2018). In contrast to a material coherent structure such as the polar cap patch, a fluid coherent structure is a feature in the flow that persists over some amount of space and time (Venditti et al., 2013). A fluid coherent structure may be defined as observed from an Eulerian frame, in which the flow moves past a fixed observer, or a Lagrangian frame, in which the observer moves with the flow. As an example of the Eulerian and Lagrangian definitions of coherent structures, consider a hurricane: an Eulerian definition such as vorticity would help define the eye of the hurricane, while a Lagrangian definition, which is the subject of this work, will define the perimeter of the hurricane (du Toit & Marsden, 2010).

As in Wang et al. (2018), we search for the Lagrangian coherent structure, which is defined as a manifold (a surface in a 3-D flow, or a ridge in a 2-D flow) that is the locus of maximal separation in a time-evolving flow (Haller, 2015). Because LCSs are frame-invariant, they are appropriate for turbulent time-varying fluid flows such as the ionosphere (Wang et al., 2018). In addition, LCSs may be useful to study polar cap patches because they may allow us to predict where material in a flow may or may not be transported (Peacock & Haller, 2013). Previous work has found LCSs in the ionosphere-thermosphere (IT) system using empirical models for the ionosphere (Wang et al., 2018) and thermosphere (Wang et al., 2017). Wang et al. (2018) found that the LCS in the high-latitude ionosphere is a horseshoe- ("U-") shaped structure surrounding the pole with the closed end oriented toward the dayside. The horseshoe LCS responds to geomagnetic activity by expanding equatorward. Their comparison of the polar cap patch with the location of the LCS found that a patch forms from plasma that is poleward of the dayside LCS.

The prior work on ionospheric LCSs relied on the Weimer high-latitude potential empirical model (Weimer, 2005). The Weimer model is a function of the IMF conditions and must be used with caution when using IMF input that is greater than the largest IMF used to derive the model (Weimer, 2005), which was the case during the 17 March 2015 polar cap patch study in Wang et al. (2018). In addition, empirical models may be unable to predict substorm variations or small-scale fluctuations (Khazanov, 2016). Therefore, data-driven $\vec{E} \times \vec{B}$ ion drifts may be better suited to search for LCSs since they may be able to corroborate and provide other insights about ionospheric flow that were missed by the model.

The Super Dual Auroral Radar Network (SuperDARN) is a collection of high-frequency radars located over the middle-to-high polar latitudes in both hemispheres (Chisham et al., 2007). The radar's line of sight ion drift measurements are combined with a statistical model by fitting the data to an expansion of the electric potential in terms of spherical harmonics functions (Gjerloev et al., 2018; Ruohoniemi & Baker, 1998). The statistical model depends on the IMF conditions (Cousins & Shepherd, 2010; Ruohoniemi & Greenwald, 1996; Shepherd & Ruohoniemi, 2000, 2005) and is used to fill the gaps wherever data are not available. The final products are the $\vec{E} \times \vec{B}$ ion drift velocities and the electric potential over a global high-latitude grid in both hemispheres. The work of Moen et al. (2013) demonstrated that the SuperDARN convection flows

can be used to track polar cap patches backward and forward in time, making them appropriate to search for LCSs.

In this work, we will use SuperDARN-derived $\vec{E} \times \vec{B}$ ion drift fields to find LCSs in the ionosphere. We assume that the plasma fluid is a single species and use flow fields describing plasma motion. As with the ionospheric LCS study of Wang et al. (2018), in this work we assume that the plasma drift and, thus, the motion of polar cap patches is horizontal and governed by $\vec{E} \times \vec{B}$ drift. These are reasonable assumptions in the high latitudes due to the absence of vertical shears (Anderson et al., 1996; Kirchengast, 1996). This work strives to answer the following questions: What are the LCSs derived from SuperDARN data during quiet and storm periods? How do they compare with those from models? Does the necessary condition found by Wang et al. (2018), that patches form from plasma that is poleward of the dayside LCS, still hold? The paper is divided as follows: in section 2, we review background on the calculation of LCSs; in section 3, we compare LCSs during storm and quiet periods and LCSs from models and data; in section 4, we study the formation and propagation of polar cap patches; and we conclude in section 5.

2. Background: LCS Computation

A commonly used method of finding LCSs is by computing the finite-time Lyapunov exponent (FTLE). Lyapunov exponents are most commonly used in the analysis of dynamical systems, as they describe the time evolution of system trajectories in phase space. For example, when a dynamical system is linearized about an equilibrium point, under certain conditions negative Lyapunov exponents indicate that the nonlinear system is stable for perturbations away from that equilibrium (Pikovsky & Politi, 2016). The finite-time Lyapunov exponent is computed over a finite-time interval specifically. Dynamical systems theory concepts can be applied to analyze coherence in velocity fields (Haller, 2015). In effect, fluid particles in a physical flow field could exhibit motion such as that of a fixed point, or periodic orbit. In time-varying flows, the FTLE value measures the separation tendency between particles after a given period of time, and the LCS is defined as the $N-1$ dimensional surface (i.e., a 1-D ridge in a 2-D flow) of the locally maximum FTLE values (Shadden et al., 2005).

In order to find the LCSs, we use the Ionosphere-Thermosphere Algorithm for Lagrangian Coherent Structures (ITALCS; Wang et al., 2018). ITALCS uses 2-D flow fields as inputs and computes the finite-time Lyapunov exponent (FTLE) values (Wang et al., 2018). To compute the FTLE value of each fluid element, a 2-D grid of particles equally spaced by δ_x in one direction and δ_y in the second direction at the start time t_0 is initialized. A 2-D flow field is provided from t_0 to $t_f = t_0 + \tau$, at Δt intervals, where τ is the integration time. In Figure 1 (Wang, 2018), we illustrate how the FTLE value is calculated for one particle: the blue star in Figure 1a, which has four neighboring particles: black and yellow dots separated by $2\delta_x$ from each other; and red and green dots separated by $2\delta_y$ from each other. Using the flow fields, each particle's position is integrated forward in time to get the particle's final position at t_f. The matrix $\mathbf{J}$, which quantifies the amount of stretching that occurs, can then be obtained using equation (1) below, where $\Delta x(\tau)$ is the change in the x position of the two horizontal neighboring particles and $\Delta y(\tau)$ is the change in the y position of the vertical neighboring particles as shown in Figures 1b and 1c.

$$\mathbf{J} \equiv \begin{bmatrix} \frac{\Delta x(\tau)}{|2\delta_x|} & \frac{\Delta x(\tau)}{|2\delta_y|} \\ \frac{\Delta y(\tau)}{|2\delta_x|} & \frac{\Delta y(\tau)}{|2\delta_y|} \end{bmatrix} \tag{1}$$

The FTLE value σ is calculated as the normalized maximum eigenvalue of the Cauchy-Green Deformation Tensor ($\mathbf{J}^T\mathbf{J}$) as shown in equation (2) below.

$$\sigma(\mathbf{J}) = \frac{1}{|\tau|} \log\left(\sqrt{\lambda_{\max}((\mathbf{J}^T\mathbf{J}))}\right) \tag{2}$$

More details on the FTLE calculations and the application to spherical coordinates can be found in Wang et al. (2018) and references therein.

3. LCS Comparisons: Quiet Versus Storm Periods and Models Versus Data

3.1. Method

In this section, we find LCSs from SuperDARN $\vec{E} \times \vec{B}$ drifts to (1) determine the LCS's response to geomagnetic activity, and (2) compare the LCS found from models and data. The SuperDARN gridded data product

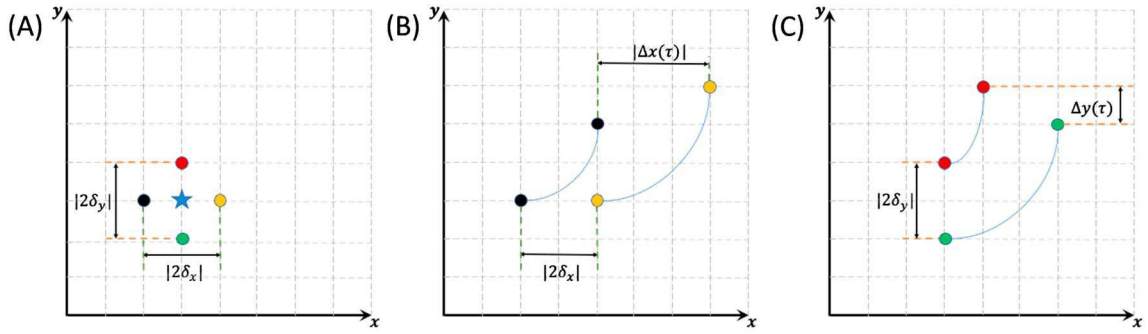

Figure 1. Schematic illustrating the FTLE value calculation at a grid point. (a) The blue star indicates the position of the grid point whose FTLE is computed. The black and yellow dots are the horizontal neighboring particles, and the red and green dots are the vertical neighboring particles. (b) The initial and final horizontal positions of the horizontal neighboring particles. (c) The initial and final vertical positions of the vertical neighboring particles.

is provided at 10-min intervals over a 2-D geomagnetic grid with geomagnetic latitudes ranging from 90°N to 50°N with $\delta_y = 1°$ spacing and geomagnetic longitudes ranging from 180°W to 178°E with $\delta_x = 2°$ spacing. The horizontal ion drifts are ground speeds provided in a geographic east-north coordinate system. In order for the drift velocities to be integrable to provide positions, the ion drifts are rotated to a magnetic east-north coordinate system using the declination angle of Earth's magnetic field, calculated from the twelfth generation of the International Geomagnetic Reference Field (IGRF-12) (Thébault et al., 2015). The ion drifts are then converted to degrees per second as shown in Wang et al. (2018). The horizontal $\vec{E} \times \vec{B}$ ion drift flow fields in units of degrees per second are then used as inputs into ITALCS. We use the SuperDARN $\vec{E} \times \vec{B}$ ion drifts as inputs to ITALCS to generate the FTLE maps and identify the LCS structures.

For the two investigations, we select the same geomagnetically quiet and stormy periods as Wang et al. (2018). The quiet period is 16 March 2015 with $t_0 = 12{:}00$ UT and $t_f = 15{:}00$ UT; the storm period is 17 March 2015 with $t_0 = 12{:}00$ UT and $t_f = 15{:}00$ UT with a $\Delta t = 10$ min and $\tau = 3$ hr and the same spatial grid as the SuperDARN data. The AE index, which is a measure of auroral electrojet geomagnetic activity, during these periods is shown in Wang et al. (2018). The IMF conditions at 10-min intervals are shown in Figures 2a and 2b, obtained from the OMNI database (King & Papitashvili, 2005). Figure 2c will be discussed in section 4. The IMF is in a geocentric solar magnetospheric (GSM) reference frame, in which the x axis points toward the Sun, the z axis points toward the magnetic north pole (positive = north), and the y axis completes the right-handed basis. During the quiet period in Figure 2a, the IMF components have magnitudes less than 10 nT, and directions of $B_z > 0$, $B_y > 0$ from 12:00 UT to 12:40 UT and $B_z > 0$, $B_y < 0$ from 12:40 to 15:00 UT. During the storm period in Figure 2b, the IMF components have magnitudes between 20 and 30 nT, and directions of $B_z < 0$, $B_y > 0$ throughout the whole period except for a brief excursion northward at 13:40 UT.

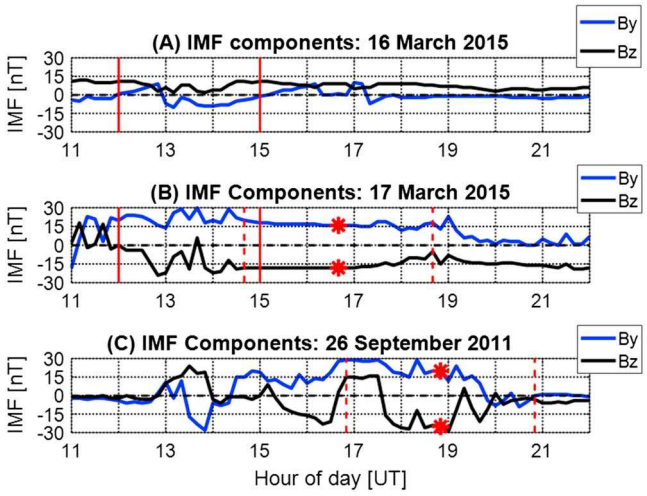

Figure 2. Interplanetary magnetic field (IMF) components for (a) 16 March 2015, (b) 17 March 2015, and (c) 26 September 2011. The solid red lines in (a) and (b) enclose the quiet and storm periods, respectively, to be used in the comparison study (section 3.2). The red stars in (b) and (c) indicate the times that patch A and patch B were identified, and the red dashed lines enclose the periods studied in the final study (section 4).

To compare storm time model LCSs to data-based LCSs, we use the Weimer model (Weimer, 2005) for high-latitude electric potential and IGRF-12 (Thébault et al., 2015) to model Earth's magnetic field with the same temporal and spatial parameters as in the first study, of $t_0 = 12{:}00$ UT, $t_f = 15{:}00$ UT, $\tau = 3$ hr, $\Delta t = 10$ min. We obtain $\vec{E}$ by numerically taking the negative gradient of the electric potential. The $\vec{E} \times \vec{B}$ drifts are then calculated in geographic east-north-up coordinates and rotated to the same reference frame as in the first study. The data-based and model-based LCSs are then compared for the storm period.

3.2. Results

Figures 3a and 3b show the FTLE values at $t_0 = 12{:}00$ UT, calculated with flows from (a) SuperDARN data during the quiet period, and (b) SuperDARN data during the storm period. The center of each plot is the

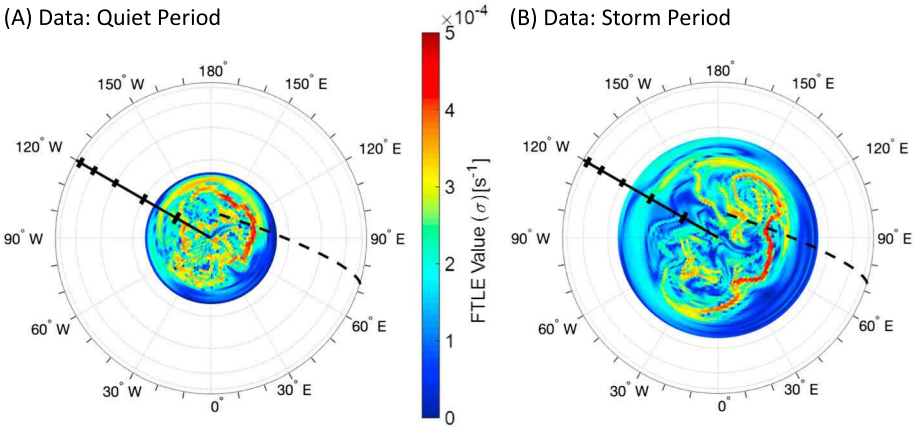

Figure 3. Super Dual Auroral Radar Network-derived finite-time Lyapunov exponent (FTLE) values in the geomagnetic northern hemisphere during the (a) quiet time and (b) storm time. The black dashed curve indicates local noon. All plots are in geomagnetic coordinates. The black tick marks at 120°W mark magnetic latitudes ranging from 90°N magnetic at the center to 15°N magnetic at the perimeter in 15° intervals.

geomagnetic north pole (the point at which the tilted-dipole axis intercepts the Earth's surface) and the coordinates are geomagnetic latitude and longitude. Local noon is marked by the black dashed curve. The color map represents the FTLE value at each position. Since the LCS is defined as the locally maximum FTLE values, the LCS structures are the red ridges.

From Figures 3a and 3b, we can compare the LCSs found with data during the quiet and storm periods, respectively. The figures show that the LCS during the storm period lies further equatorward than the quiet period (60° vs. 70°N magnetic). This can be attributed to the IMF conditions. Because the B_z component was southward during the storm period, the electric potential pattern is more equatorward, and thus, so is the LCS. This is shown in the videos in the supporting information, in which we show the electric potential pattern from SuperDARN during the quiet and storm periods, respectively.

In addition, Figures 3a and 3b also show that the LCS for the storm and quiet periods do not have the horseshoe-like (U) shape found by Wang et al. (2018). In fact, the quiet-time LCS red ridge is simply a latitudinal band spanning approximately 130° in longitude. This is likely related to the fact that the electric potential pattern during this time span does not have two electric potential cells. As shown in the video in the supporting information, during the 3-hr quiet period investigated, the electric potential is just a dominant

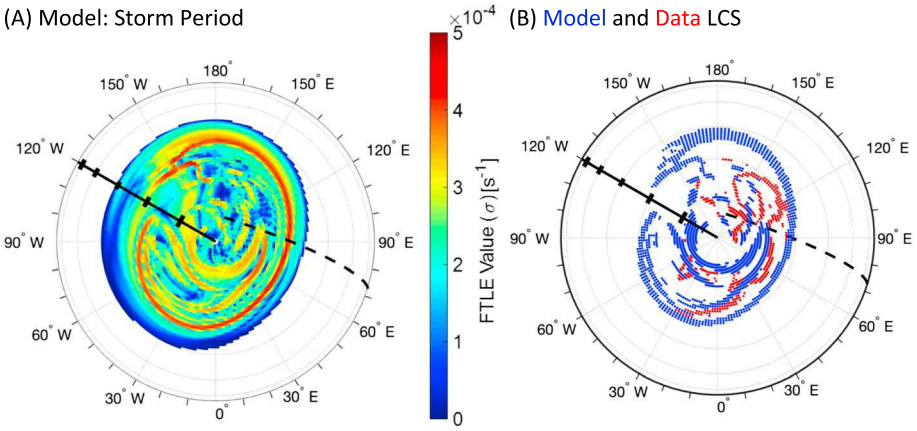

Figure 4. Geomagnetic northern hemisphere (a) FTLE map from the Weimer and IGRF-12 models during the storm period. (b) A comparison of the model LCSs (blue) and data LCSs (red), identified as the locus of points at which the FTLE values exceed 3×10^{-4} s^{-1}. The black dashed curve indicates local noon. The black tick marks at 120°W mark magnetic latitudes ranging from 90°N magnetic at the center to 15°N magnetic at the perimeter in 15° intervals. FTLE = finite-time Lyapunov exponent; IGRF-12 = twelfth generation of the International Geomagnetic Reference Field; LCS = Lagrangian Coherent Structure.

negative cell, which is common for a positive IMF B_z and negative IMF B_y (Ruohoniemi & Greenwald, 1996). It is likely that, because the two-cell electric potential pattern broke down, the LCS is not U-shaped. From these observations, we conclude that the high-latitude ionospheric LCS is dependent on the IMF conditions.

Next, we compare the LCS found from models and from data during the storm period. Figure 4a shows the FTLE map calculated with flows from models (Weimer 2005 and IGRF-12). Figure 4b is a map comparing the Weimer model (blue) and SuperDARN (red) storm-time LCSs. Each LCS is identified by marking a dot at the gridpoints lying on the LCS ridges ($\sigma > 3 \times 10^{-4}$ s^{-1}). In the third video in the supporting information, we show the electric potential from the Weimer 2005 models during the 3-hr storm period.

On Figure 4b, the equatormost model-based LCS (blue) is a horseshoe-like structure that has slow variation in its latitude with longitude. The most equatorward data-based horseshoe-like structure (red) has significant latitudinal variation with longitude, appearing more as a "W" than a "U." The cause of the W shape as opposed to the U shape may be due to the changes in the electric potential over time, as seen in the videos in the supporting information. During the 3-hr storm period the Weimer 2005 model showed a consistent two-cell electric potential pattern with little to no change through time, while with SuperDARN, the two-cell electric potential was not persistent. For example, the electric potential at 12:00 UT was a dominant negative cell, at 12:40 UT a two-cell pattern, at 13:20 UT multiple cells, and after 14:00 UT a distorted two-cell pattern. We hypothesize that these multiple changes pull the LCS away from the pure U shape.

In addition, the Weimer model LCS has a greater longitudinal span than the SuperDARN LCS. From Figure 4b, we can visually identify that the model-based horseshoe extends from 115°W eastward to 125°W, spanning 350° in magnetic longitude around the globe. The data-based horseshoe only extends from 30°W to 165°E, spanning 195° in magnetic longitude. This means that the SuperDARN-derived convection shows that the particles have weak separation on the nightside and strong separation on the dayside, while the model shows that there is strong separation almost around the globe.

Also, the data-based horseshoe has a latitudinal position that is always poleward of the model-based horseshoe. Between 30°W and 120°E, the latitudinal difference in the LCS ridge location is about 5°. The latitudinal difference at 150°E is about 10° (59°N vs. 49°N). This may indicate that either the Weimer 2005 model overestimated or SuperDARN underestimated the expansion of the two-cell pattern for this storm, or some combination of the two. Weimer 2005 may have overestimated the expansion of the electric potential pattern since it is a storm for which the IMF conditions exceed normal conditions, which may limit the model's accuracy (Weimer, 2005). SuperDARN may have underestimated the expansion of the electric potential pattern since (1) the true expansion may be outside of the radar field of view (Baker et al., 2007) and (2) the SuperDARN electric potential fit makes use of the Heppner-Maynard boundary, which allows the velocities to be set to zero below some low-latitude boundary (Gjerloev et al., 2018).

4. LCS Application: Formation and Propagation of a Polar Cap Patch

4.1. Method

For the final study, we use two previously identified polar cap patches to see if there is a relationship between the LCS location and the formation and propagation of polar cap patches. The first patch was identified by Wang et al. (2018) as occurring on 17 March 2015 at 16:40 UT using MIDAS. The second patch was identified by Zhang et al. (2013) as occurring on 26 September 2011 at around 18:50 UT using Global Positioning System (GPS) TEC data from an extensive array of receivers. We will refer to the polar cap patch on 17 March 2015 as patch A, and the one on 26 September 2011 as patch B. In this paper, patch A is used to compare SuperDARN LCSs with those found by Wang et al. (2018). Patch B is used to determine whether the observations found regarding polar cap patches are consistent for more than one polar cap patch.

To study patches A and B, we use MIDAS TEC maps for 17 March 2015 and 26 September 2011. MIDAS obtains global TEC maps by performing a three-dimensional, time-dependent electron density inversion of GPS slant TEC measurements (Chartier et al., 2012; Mitchell & Spencer, 2003; Spencer & Mitchell, 2007). In Figure 5a we plot the TEC from MIDAS for 17 March 2015 at 16:40 UT. The location of the patch is indicated by the red box. The plot is in geographic coordinates, where the center of the plot is the north pole and the bottom of the plot is local noon. The color bar represents the vertical TEC in TEC units (TECu).

The IMF conditions during this period are shown in Figure 2b, with 16:40 UT marked by the red star. During the 2 hr before and after patch A was identified (red dashed lines in Figure 2b), the IMF was $B_z < 0, B_y > 0$.

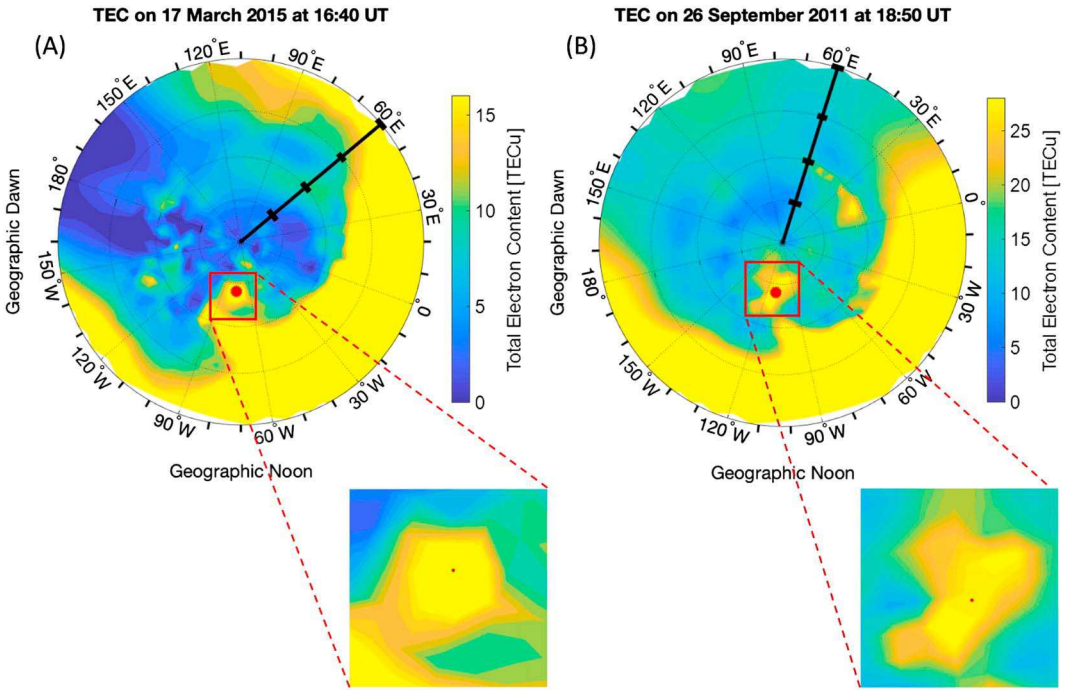

Figure 5. Geographic northern hemisphere (a) total electron content (TEC) map in TEC units (TECu) derived from MIDAS on 17 March 2015 at 16:40 UT. (b) TEC map derived from MIDAS on 26 September 2011 at 18:50 UT. The approximate center of each patch is indicated by the red dot (see insets). The north pole is at the center of each plot and local noon at the bottom. The black tick marks on 60°E mark latitudes ranging from 90°N at the center to 30°N at the perimeter in 15° intervals. MIDAS = Multi-Instrument Data Analysis System.

Based on the results from the previous section, we expect this will correspond to a two-cell convection cell and a W-shaped LCS. In Figure 5b, we show the MIDAS TEC for 26 September 2011 at 18:50 UT in the same format as Figure 5a, over the northern hemisphere. The IMF conditions during this period are shown in Figure 2c, with 18:50 UT marked by the red star. During the 2 hours before and after patch B was identified (red dashed lines in Figure 2c), the IMF was $B_z < 0$, $B_y > 0$ except: $B_z > 0$ at 16:50–17:30 UT and at 19:20 UT; and $B_y < 0$ at 19:50–20:50 UT. Based on previous literature such IMF conditions will also correspond to a two-cell convection cell (Ruohoniemi & Greenwald, 1996) and thus we anticipate a W-shaped LCS.

First, we show that MIDAS is actually reconstructing patches by comparing to electron density measurements from the Defense Meteorological Satellite Program (DMSP). Each DMSP satellite has a Sun-synchronous orbit at an altitude of about 840 km. A Langmuir probe is used to measure the in situ electron density (Greenspan et al., 1986). In Figure 6a, we plot the MIDAS TEC plot on 17 March 2015 16:50 UT with the ground track of the F15 DMSP satellite from 16:50 UT to 17:00 UT at 1-min intervals. Figure 6b shows the electron density obtained from DMSP. The *x* axis is the time of the measurement, increasing from right to left to correspond with the right-to-left motion in Figure 6a along the satellite's ground track. Looking at the density plot in Figure 6b from right to left, we can see that there is high electron density from 16:50 UT to 16:51 UT, followed by low electron density from 16:51 UT to 16:57, then high electron density from 16:57 UT to 16:59 UT, and finally moderate electron density from 16:59 to 17:00 UT. The electron density from DMSP matches fairly well with the MIDAS reconstruction and thus gives strong evidence that MIDAS is reconstructing a polar cap patch.

Similarly, Figure 6c shows the MIDAS TEC for 26 September 2011 at 19:00 UT with the location of F17 DMSP satellite from 19:00 UT to 19:10 UT. The DMSP satellite traverses the map from right to left. In Figure 6d, we show the electron density obtained from DMSP. The *x* axis is time of measurement, increasing from right to left to correspond to the satellite motion right to left in the map in Figure 6c. In this case, looking from right to left we can see low electron density from 19:00 UT to 19:03 UT, followed by high electron density from 19:03 to 19:06, and finally low electron density from 19:06 UT to 19:10 UT. Again the electron density from

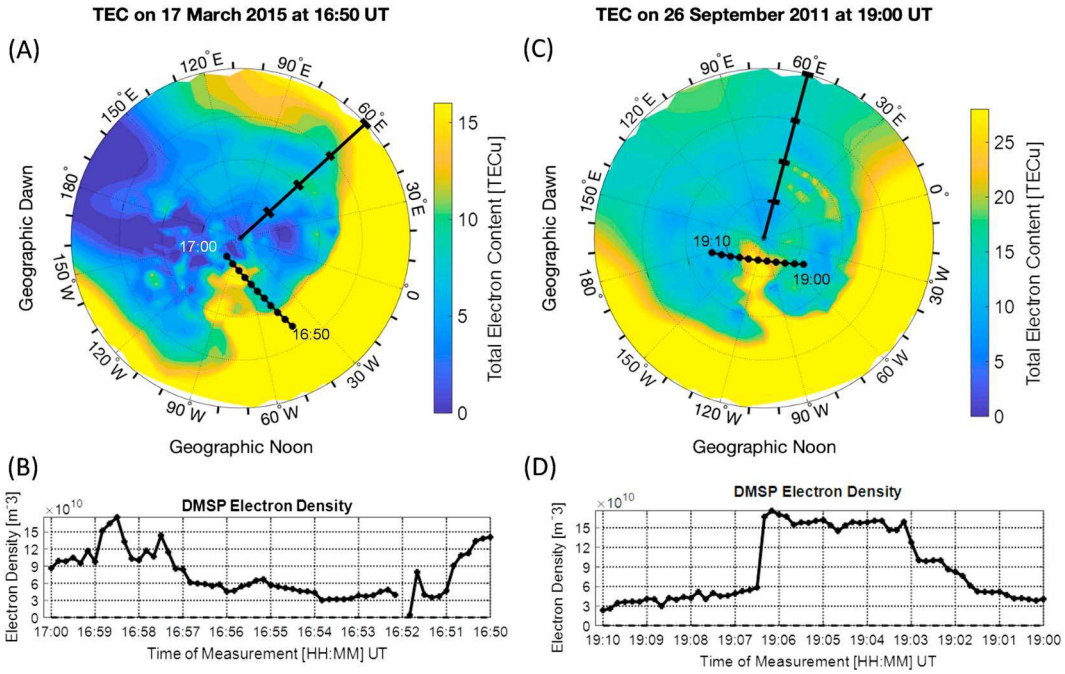

Figure 6. (a) MIDAS TEC plot on 17 March 2015 at 16:50 UT with the position of the F15 DMSP satellite over 10 min marked by black dots at 1-min intervals. (b) Electron density from DMSP on 17 March 2015 at 16:50 UT to 17:00 UT from right to left. (c) MIDAS TEC plot on 26 September 2011 at 19:00 UT with the position of the F17 DMSP satellite over 10 min marked by black dots at 1-min intervals. (d) Electron density from DMSP on 26 September 2011 at 19:00 to 19:10 UT from right to left. In (a) and (c), the black tick marks at 60°E mark geographic latitudes ranging from 90°N at the center to 30°N at the edge of plot in 15° intervals. In (b) and (d) the *x* axis is the time of the measurement increasing from right to left, to correspond with the right-to-left motion along the satellite's ground track. MIDAS = Multi-Instrument Data Analysis System; TEC = total electron content; DMSP = Defense Meteorological Satellite Program; SuperDARN = Super Dual Auroral Radar Network.

DMSP matches well with the MIDAS reconstruction, which suggests that MIDAS accurately reconstructed a polar cap patch.

Next, we assess the accuracy of the SuperDARN-gridded drift velocity data product at the location of the polar cap patches by comparing it with ion drift velocity measurements from DMSP. The DMSP satellite uses an ion drift meter (IDM) to measure the drift velocity perpendicular to the satellite motion and the drift velocity vertically upward (Hardy et al., 1984). In Figure 7a, we show the TEC map from Figure 6a zoomed in on the satellite track with ion drift vectors overplotted for 17 March 2015 at 16:50 UT to 17:00 UT from DMSP (black), SuperDARN (red), and the Weimer 2005 and IGRF-12 models (blue). The SuperDARN velocity at the grid point closest to each DMSP location is plotted. To see how the magnitudes compare, in Figure 7b, we show the eastward component of the ion drift and in Figure 7c the northward component. The black curve is from DMSP, red curve from SuperDARN, and blue curve from the Weimer 2005 and IGRF-12 models. The *x* axis is the time of the measurement increasing from right to left, to correspond with the right-to-left motion along the ground track plotted in Figure 7a.

From these plots, we can see that in the time around passage through the polar cap patch (16:55–17:00 UT), the velocities from the three sources appear to be consistent in direction and magnitude, with the velocities differing by values up to 250 m/s. In the area equatorward of the patch (16:50–16:54 UT), the velocities from both SuperDARN and Weimer disagree in both magnitude and direction from DMSP. Specifically, in the zonal direction, the DMSP data show a shift from westward to eastward convection from 16:51:50 UT to 16:52:30. This corresponds to lower latitudes of 57.9–60.1°N along the DMSP ground track. The shear from westward convection of 1,700 m/s to eastward convection of 400 m/s is large in magnitude, over a minute of duration. It is likely that this shear, if sustained, is a significant contributor to fluid separation, and thus higher FTLE values. Meanwhile, SuperDARN shows a gradual shift from 800 m/s westward at 16:53:30 UT (63.4° latitude) to about 400 m/s eastward at 16:56 UT. Weimer also shows a gradual shift, from −1,500 m/s at 16:53 UT (63° latitude) to about 250 m/s eastward at 16:56 UT. Similarly, neither SuperDARN nor Weimer

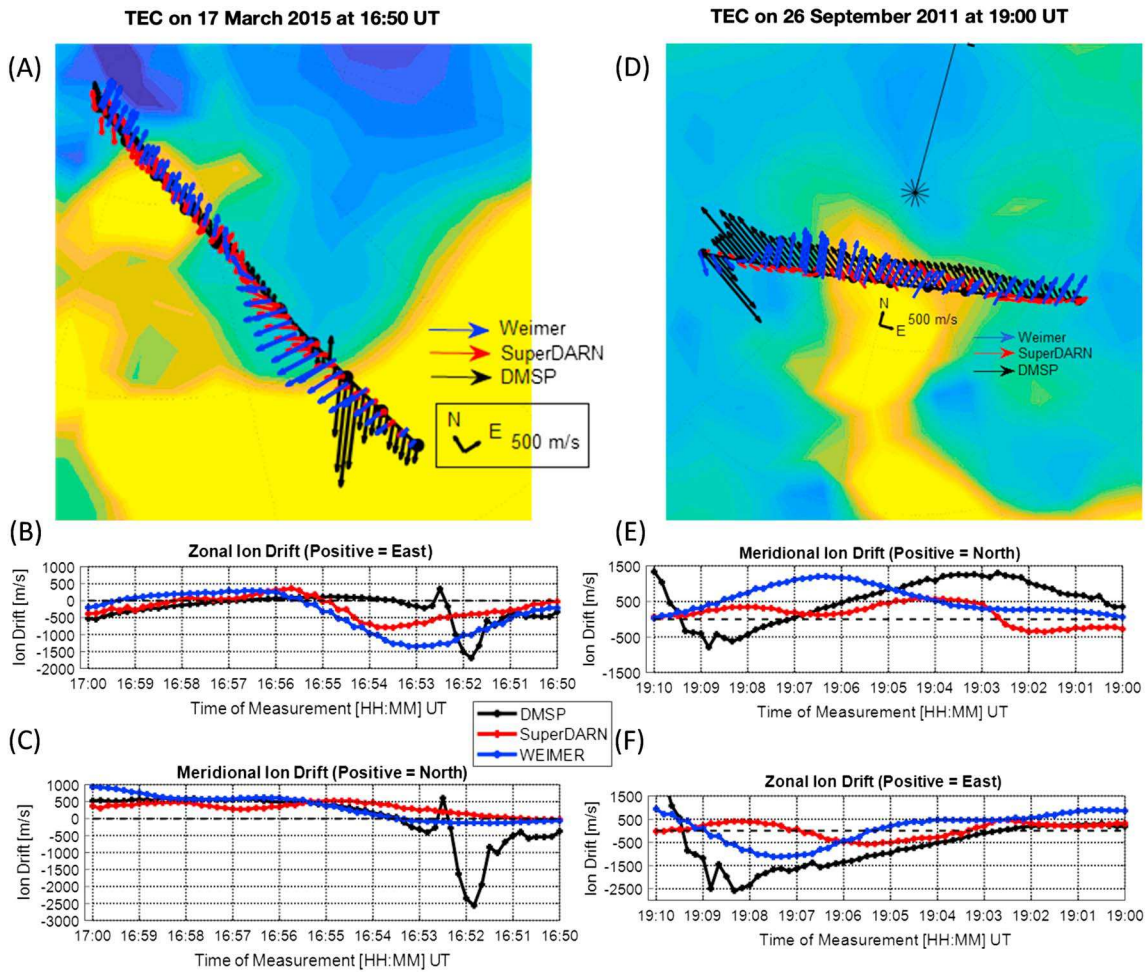

Figure 7. (a) Zoomed in map of MIDAS TEC on 17 March 2015 at 16:50 UT and DMSP ground track, with ion drift vectors overplotted. (b) Eastward and (c) northward drift components on 17 March 2015 at 16:50 UT to 17:00 UT. (d) Zoomed in map of MIDAS TEC on 26 September 2011 at 19:00 UT and DMSP ground track, with ion drift vectors overplotted. (e) Eastward and (f) northward drift components on 26 September 2011 at 19:00 UT to 19:10 UT. The black arrows/curve are DMSP measurements, red from the SuperDARN grid point closest to the point on the DMSP ground track, and blue from the Weimer 2005 and IGRF-12 models. In (b), (c), (e), and (f), the *x* axis is the time of the measurement increasing from right to left, to correspond with the right-to-left motion along the satellite's ground track. MIDAS = Multi-Instrument Data Analysis System; TEC = total electron content; DMSP = Defense Meteorological Satellite Program; SuperDARN = Super Dual Auroral Radar Network; IGRF-12 = twelfth generation of the International Geomagnetic Reference Field.

show the meridional speed reduction that DMSP shows from 16:51:50 to 16:52:30 UT. If the smoothness of the SuperDARN and Weimer convection is a sustained bias over the FTLE integration period, this means that both SuperDARN and Weimer may underestimate the magnitude of the FTLEs. Also, in this particular case, they may also estimate the LCSs somewhat poleward of the actual location since the zonal shear is poleward of that measured by DMSP. It is important to note that at the lower latitudes, where there is the biggest disagreement, DMSP zonal and meridional components could have a relatively large contribution from the *B*-parallel ion motion, while SuperDARN only measures *B*-perpendicular drifts.

In the case of patch B, in Figure 7d we show the TEC map and ion drift vectors for 26 September 2011 at 19:00 UT to 19:10 UT, and in Figures 7e and 7f the magnitude of the east and north component of the ion drifts. They are in the same format as Figures 7a–7c, respectively. From Figure 7d, we see that Weimer shows ion drifts with a different direction than both DMSP and SuperDARN. SuperDARN and DMSP show ion drifts that are fairly consistent in direction, especially within the patch. However, the magnitudes of both SuperDARN and Weimer ion drifts are smaller than the DMSP drifts, particularly on the dawnside (left) of the ground track. In Figures 7e and 7f, the DMSP data show strong zonal and meridional shear from about 19:09–19:10 UT that is not modeled by Weimer or SuperDARN. Again this may indicate an underestimation

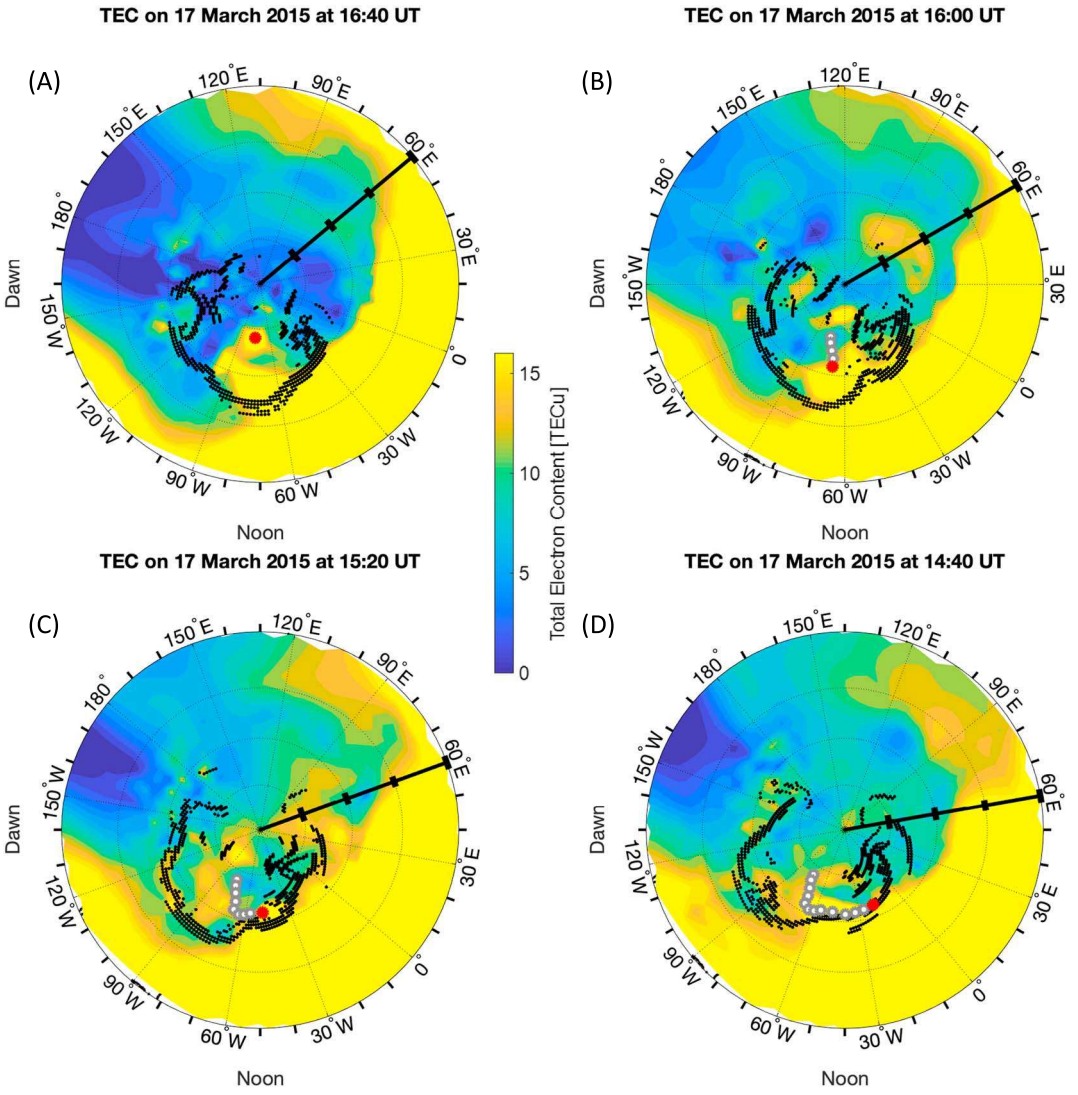

Figure 8. MIDAS total electron content (TEC) maps of the northern hemisphere on 17 March 2015 at (a) t_0 = 16:40 UT, (b) t_0 = 16:00 UT, (c) t_0 = 15:20 UT, and (d) t_0 = 14:40 UT. Local noon is at the bottom of each map. The black tick marks at 60°E mark latitudes ranging from 90°N at the center to 30°N at the edge of plot in 15° intervals. The red circle marks the current position, and the gray circles mark the subsequent positions. The black points mark the location of the LCS, which are the grid points at which the FTLE values obtained from SuperDARN drifts exceed 3×10^{-4} s^{-1} at that t_0. MIDAS = Multi-Instrument Data Analysis System; LCS = Lagrangian Coherent Structure; FTLE = finite-time Lyapunov exponent; SuperDARN = Super Dual Auroral Radar Network.

of the magnitude of the FTLE when we use SuperDARN to find LCSs. In other words, if an LCS appears with SuperDARN it may be a weaker LCS than the actual storm time drift field actually contains. Since the magnitudes of the DMSP drifts are greater than the SuperDARN drifts there may be greater separation in the true flow. We keep these caveats in mind as we proceed with the LCS analysis of patches.

First, we search for a relationship between the LCS location and the formation of polar cap patches. To do this, forward-time FTLE maps are generated from SuperDARN $\vec{E}\times\vec{B}$ drift velocities with a t_0 varying from the time each polar cap patch was identified to 2 hr before. For each t_0 we select $\tau = 3$ hr integrating forward in time with $\Delta t = 10$ min and the same spatial grid as the SuperDARN data. We then set a tracer point located at the approximate center of each polar cap patch to trace their positions backward in time to determine the origin of each of the polar cap patches. For patch A, a tracer is set at (72°N, 75°W), marked as the red dot in Figure 5a. Similarly for patch B, a tracer is set at (72°N, 110°W) marked as the red dot in Figure 5b. We then compare the tracer points' locations to the LCSs ridges to determine if there is any relationship

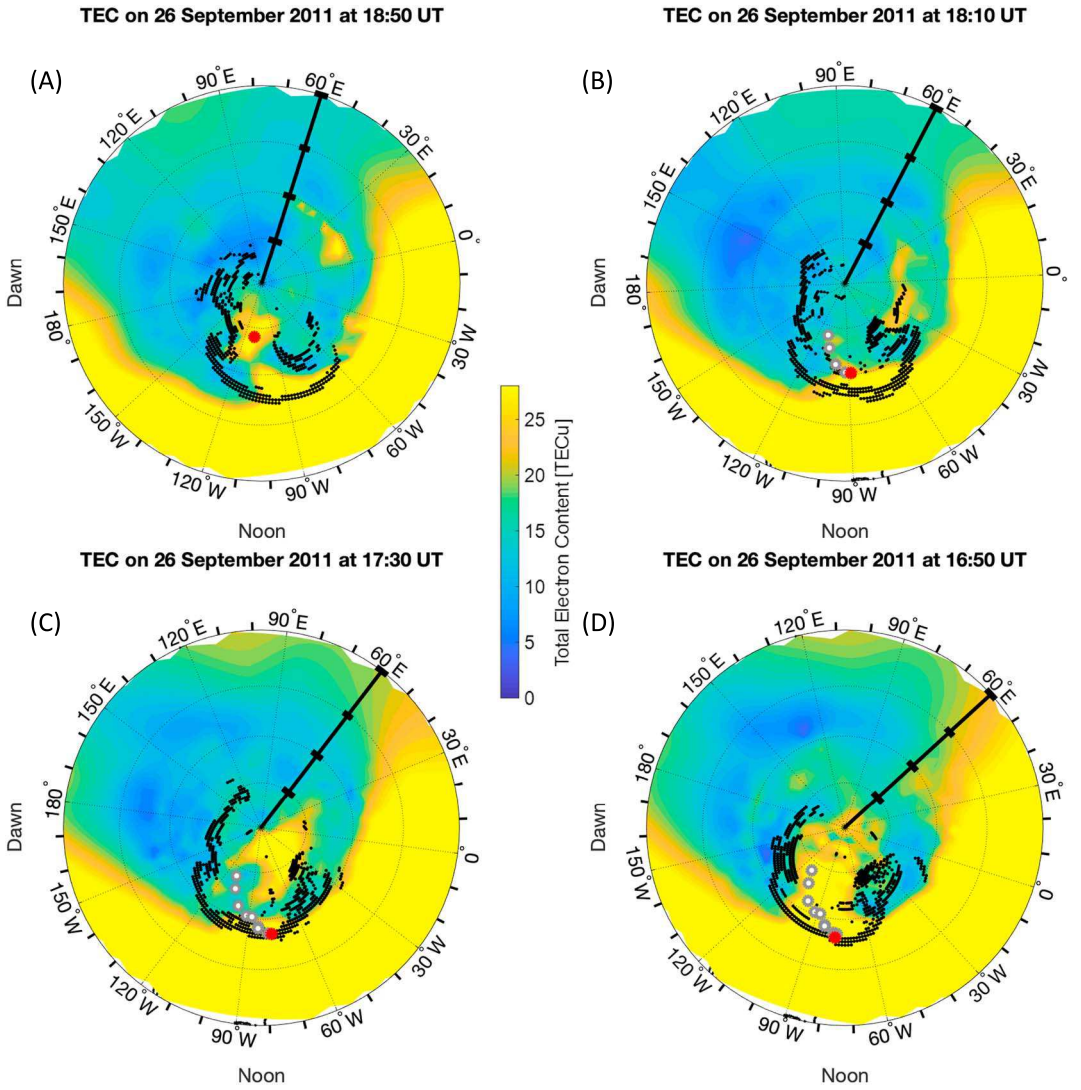

Figure 9. MIDAS total electron content (TEC) maps of the northern hemisphere on 26 September 2011 at (a) t_0 = 18:50 UT, (b) t_0 = 18:10 UT, (c) t_0 = 17:30 UT, and (d) t_0 = 16:50 UT. Local noon is at the bottom of each map. The black tick marks at 60°E mark latitudes ranging from 90°N at the center to 30°N at the edge of plot in 15° intervals. The red circle marks the current position, and the gray circles mark the subsequent positions. The black points mark the location of the LCS, which are the grid points at which the FTLE values obtained from SuperDARN drifts exceed 3×10^{-4} s^{-1} at that t_0. MIDAS = Multi-Instrument Data Analysis System; LCS = Lagrangian Coherent Structure; FTLE = finite-time Lyapunov exponent; SuperDARN = Super Dual Auroral Radar Network.

between them, (i.e., to determine whether patches form from plasma that is poleward of the dayside LCS, as Wang et al., 2018 found).

Next, we search for a relationship between the LCS location and the propagation of polar cap patches. To do this, FTLE maps are generated from SuperDARN $\vec{E} \times \vec{B}$ drift velocities with a t_0 varying from the time each polar cap patch was identified to 2 hr after with $\tau = 3$ hr, $\Delta t = 10$ min, and the same spatial grid as the SuperDARN data. The tracer points are traced forward in time for 2 hr to indicate the approximate site to which each patch might propagate according to SuperDARN-based convection.

4.2. Results

First, we analyze the formation of patch A. Figure 8 shows the TEC estimates from MIDAS on 17 March 2015 starting at t_0 = 16:40 UT in Figure 8a going back in time at 40-min intervals until t_0 = 14:40 UT in Figure 8d. The black points mark the location of the LCS for each t_0, which we define as the points at which the FTLE values obtained from SuperDARN convection have $\sigma > 3 \times 10^{-4}$ s^{-1}. The red dot is the current

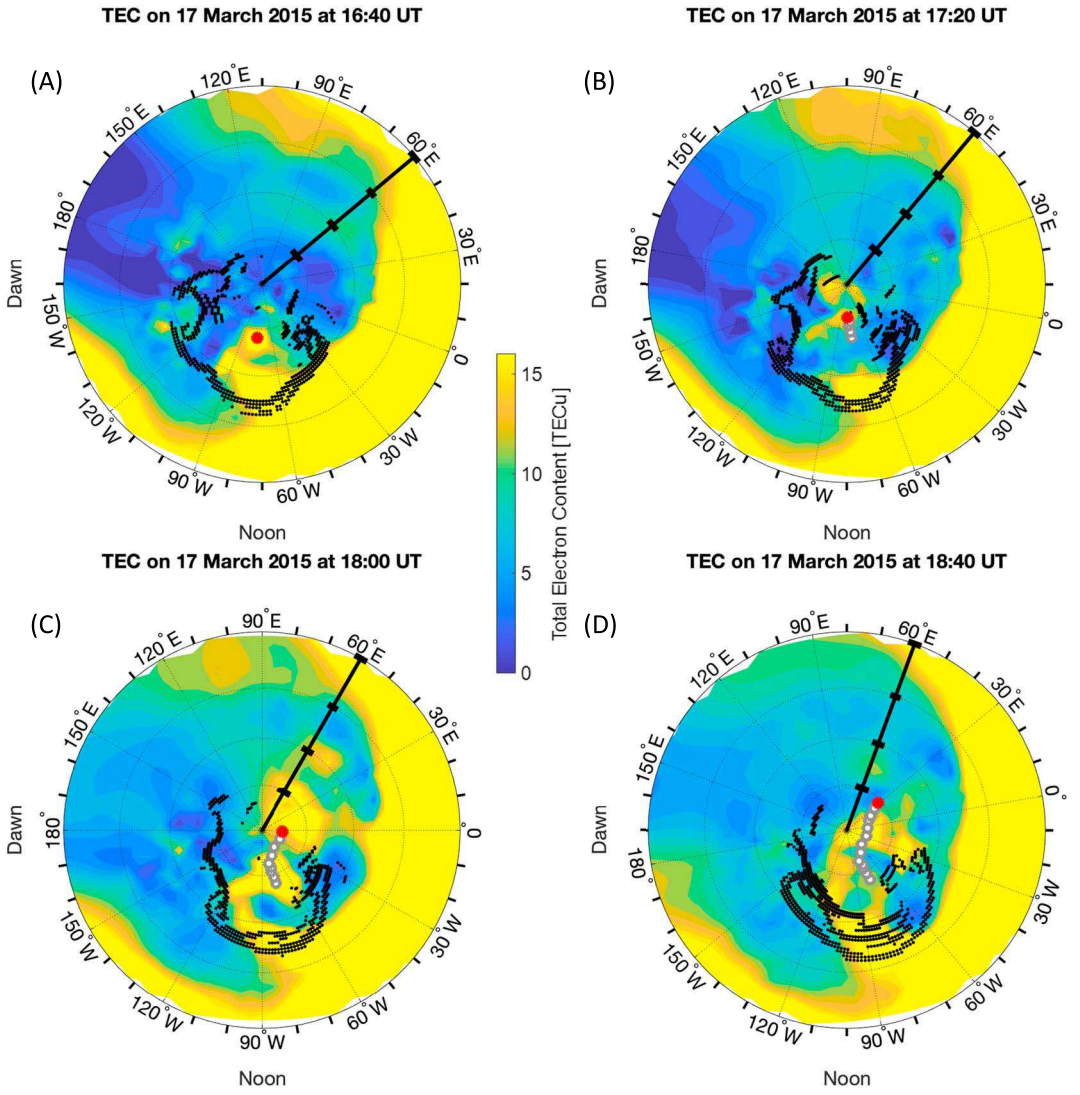

Figure 10. MIDAS total electron content (TEC) maps of the northern hemisphere on 17 March 2015 at (a) t_0 = 16:40 UT, (b) t_0 = 17:20 UT, (c) t_0 = 18:00 UT, and (d) t_0 = 18:40 UT. Local noon is at the bottom of each map. The black tick marks at 60°E mark geographic latitudes ranging from 90°N at the center to 30°N at the edge of plot in 15° intervals. The red circle marks the current position, and the gray circles mark the previous positions. The black dots indicate the location of the LCS, which are the grid points at which the FTLE values obtained from SuperDARN drifts exceed 3×10^{-4} s^{-1} at that t_0. MIDAS = Multi-Instrument Data Analysis System; LCS = Lagrangian Coherent Structures; FTLE = finite-time Lyapunov exponent; SuperDARN = Super Dual Auroral Radar Network.

location of the tracer point, and the gray dots are the positions between the current time and 16:40 UT. The positions of the tracer points at 14:40 UT in Figure 8d are (63.9°N, 19.3°W). This is consistent with Bust and Crowley (2007), which found that polar cap patches originate from plasma found in the morning and evening cells around 62°N. Also, we can see that the main LCS ridge has a W shape as anticipated from the results in section 3. However, the tracer point is on the main LCS ridge, which slightly disagrees with Wang et al. (2018) who hypothesized, examining this event using the Weimer model, that the patch would form from plasma that is poleward of the dayside LCS. In the case of the SuperDARN data-driven flows, the center of the patch appears to have formed from plasma that is on the dayside LCS ridge. However, as we noted from comparison of SuperDARN to DMSP, SuperDARN convection did not appear to show the strong shear that DMSP did, which we suspect is due to a subauroral polarization stream (SAPS). That strong shear is equatorward of the SuperDARN shear, so the true LCS may also be equatorward of the SuperDARN LCS.

To test whether this observation is consistent for more than one polar cap patch, the same examination of the formation of patch B is conducted. Figure 9 shows the TEC estimates from MIDAS on 26 September 2011

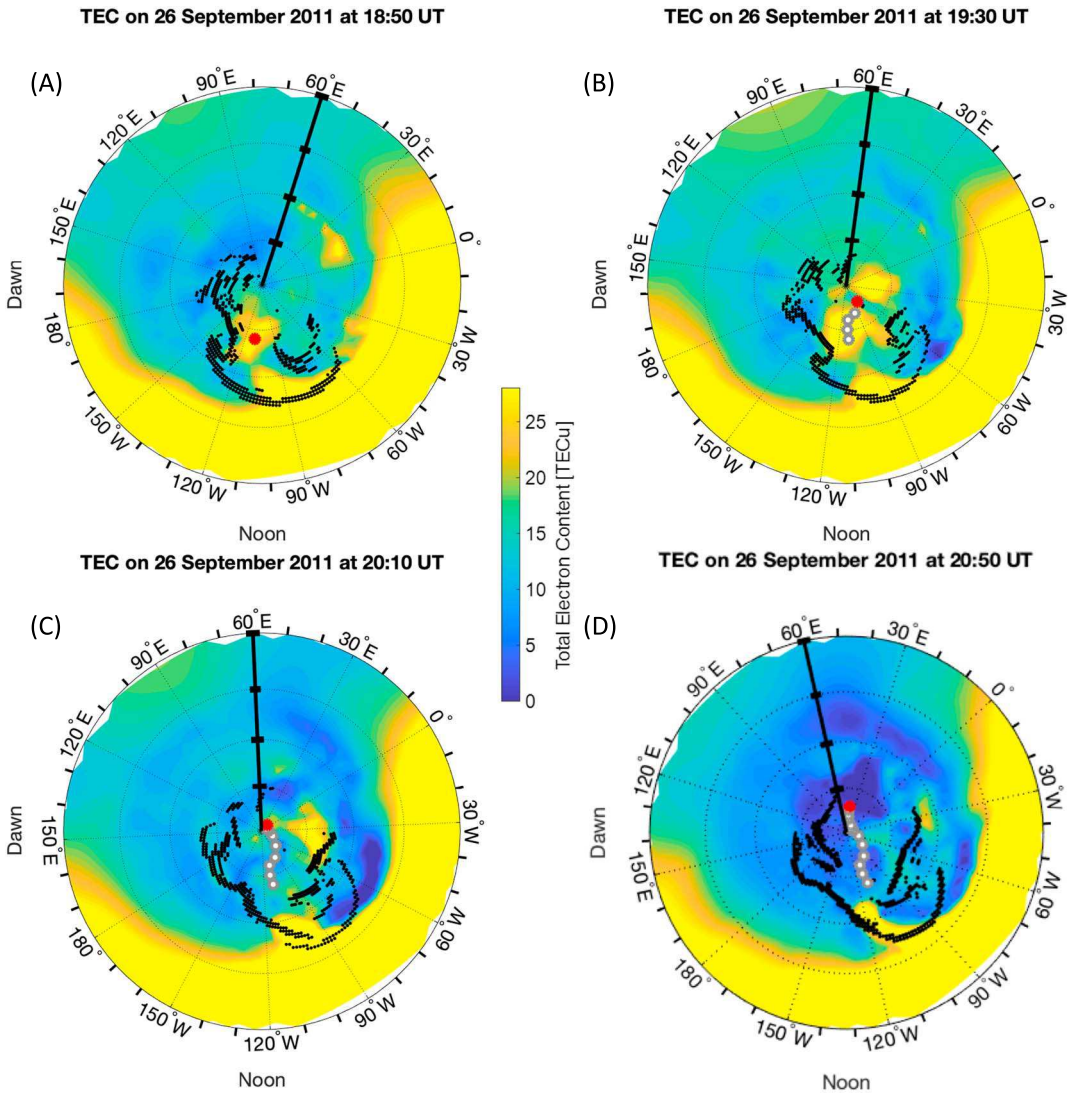

Figure 11. MIDAS total electron content (TEC) maps of the northern hemisphere on 26 September 2011 at (a) t_0 = 18:50 UT, (b) t_0 = 19:30 UT, (c) t_0 = 20:10 UT, and (d) t_0 = 20:50 UT. Local noon is at the bottom of each map. The black tick marks at 60°E mark geographic latitudes ranging from 90°N at the center to 30°N at the edge of plot in 15° intervals. The red circle marks the current position, and the gray circles mark the previous positions. The black points mark the location of the LCS, which are the grid points at which the FTLE values obtained from SuperDARN drifts exceed 3×10^{-4} s^{-1} at that t_0. MIDAS = Multi-Instrument Data Analysis System; LCS = Lagrangian Coherent Structure; FTLE = finite-time Lyapunov exponent; SuperDARN = Super Dual Auroral Radar Network.

starting at t_0 = 18:50 UT going back in time at 40-min intervals until t_0 = 16:50 UT. The plot is in the same format as Figure 8. The position of the tracer point at 16:50 UT in Figure 9d is (54.2°N, 77.7°W), which is on the main LCS ridge. This indicates that, according to SuperDARN-derived convection, the center of the polar cap patch originates from plasma that is on the main LCS ridge. In addition, the main LCS ridge is also W shaped, which was expected since the IMF conditions correspond to two-cell electric potential pattern. If we go farther back in time, the tracer continues to be on the LCS ridge (not shown).

Next, we show the propagation of patch A in Figure 10. It is in the same format as Figure 8, but with the tracer points traced forward in time from t_0 = 16:40 UT to t_0 = 18:40 UT at 40-min intervals. The position of the tracer at 18:40 UT in Figure 10d is (76.2°N, 31.3°E), which is on the dusk side at the open end of the main LCS ridge. This is consistent with the typical patch propagation scenario, which states that patches propagate from the dayside to the nightside.

Similarly, Figure 11 shows the propagation of patch B. It is in the same format as Figure 10, but with the tracer propagated forward in time from 18:50 UT to 20:50 UT at 40-min intervals. The position of the tracer at 20:50 UT in Figure 11d is (81.1°N, 40.3°E), which is also on the dusk side at the open end of the main LCS ridge. The propagation of this patch also follows the typical scenario, as it is propagating from the dayside to the nightside. By looking at the tracer locations and the MIDAS TEC estimates in Figure 11, we can see that there is a mismatch between the location of the tracer point and the actual patch. For example, in Figure 11d, we can see that the MIDAS TEC patch is located at approximately (62°N, 30°W), which corresponds to a difference of 20° in latitude and 70.3° in longitude. The mismatch may be attributed to the lack of SuperDARN radar measurement around the patch, especially westward of it. In other words the tracer position is based on a SuperDARN convection field extrapolated beyond the measurement locations (not shown, but obtainable from the SuperDARN website: vt.superdarn.org).

5. Conclusion

LCSs were found using $\vec{E}\times\vec{B}$ ion drift velocities from SuperDARN. In this work, we proposed that the shape of the LCS is directly related to the electric potential patterns, which depend on the IMF conditions. The consistent appearance of a two-cell electric potential pattern results in an approximately U-shaped LCS, as appeared in the work of Wang et al. (2018), but if the electric potential pattern is distorted throughout the period investigated, it may correspond to more of a W-shaped LCS as we showed for the geomagnetic storm event studied in section 3. The complete disappearance of a two-cell pattern caused the LCS to lose its characteristic shape. In the future, the change in shape of the LCS may be tested using global ionospheric convections from the technique developed by Gjerloev et al. (2018), which assumes that the magnetosphere-ionosphere (M-I) system has inertia that prevents the global electric pattern from changing abruptly.

The comparison between LCSs found from SuperDARN and from the Weimer and IGRF-12 models revealed that the data's LCSs were poleward and with shorter horseshoe-like structures that were more W shaped than U shaped. The study of two polar cap patches confirmed that the center of the patches originate from high-density plasma that is on the main LCS ridge. However, SuperDARN may estimate the LCS ridge in convection to be slightly weaker and further poleward than the true LCS in the flow, based on comparisons to DMSP drifts.

In this work, we assumed that plasma motion is horizontal and governed by the $\vec{E}\times\vec{B}$ ion drift. This assumption, and thus our result, is only valid for the high latitudes. A more comprehensive LCS study would need to include the other contributions to the drift discussed in Atul et al. (2018) and Sotnikov et al. (2014). Also, it is important to note that since we were looking at geomagnetic storms, there may have been a reduction in SuperDARN data capture caused by the absorption of radar signals in the ionospheric D layer (Baker et al., 2007). Finally, patch formation and propagation under different IMF B_z and B_y conditions merits further study.

Acknowledgments
This work was supported by the National Science Foundation AGS-1352602 and the Armour College of Engineering Program for Undergraduate Research Education (PURE) award. The authors acknowledge the providers of SuperDARN data. SuperDARN is a collection of radars funded by national scientific funding agencies of Australia, Canada, China, France, Italy, Japan, Norway, South Africa, United Kingdom, and the United States of America. The authors acknowledge the use of the VT SuperDARN Web site (vt.superdarn.org) for access to radar data and data products. The authors thank Daniel Weimer for the electric potential model source code. The 12th-generation International Geomagnetic Reference Field (IGRF 12) model is available at International Union of Geodesy and Geophysics (https://www.ngdc.noaa.gov/ IAGA/vmod/igrf.html). The authors thank Cathryn Mitchell of the University of Bath, U.K., for providing access to the Multi-Instrument Data Analysis System (MIDAS). The OMNI IMF data were obtained from the GSFC/SPDF OMNIWeb interface (https://omniweb.gsfc.nasa.gov). The authors acknowledge the use of DMSP data provided by Boston College via the Madrigal Database at Haystack Observatory (http://madrigal.haystack.mit.edu/madrigal/). The authors thank the reviewers and editors for their insightful and constructive comments.

References

Anderson, D. N., Buchau, J., & Heelis, R. A. (1988). Origin of density enhancements in the winter polar cap ionosphere. *Radio Science*, *23*(4), 513–519. https://doi.org/10.1029/RS023i004p00513

Anderson, D. N., Decker, D. T., & Valladares, C. E. (1996). Global theoretical ionospheric model (gtim), (R. W. Schunk)., *Solar-terrestrial energy program: Handbook of ionospheric models* (pp. 133–152). Logan, UT: Center for Atmospheric and Space Sciences.

Atul, J. K., Singh, R., Sarkar, S., Kravchenko, O. V., Singh, S. K., Chattopadhyaya, P. K., & Kaw, P. K. (2018). Magnetic shear damped polar convective fluid instabilities. *Journal of Geophysical Research: Space Physics*, *123*, 808–818. https://doi.org/10.1002/2017JA024778

Baker, J. B. H., Greenwald, R. A., Ruohoniemi, J. M., Oksavik, K., Gjerloev, J. W., Paxton, L. J., & Hairston, M. R. (2007). Observations of ionospheric convection from the wallops SuperDARN radar at middle latitudes. *Journal of Geophysical Research*, *112*, A01303. https://doi.org/10.1029/2006JA011982

Burston, R., Mitchell, C., & Astin, I. (2016). Polar cap plasma patch primary linear instability growth rates compared. *Journal of Geophysical Research: Space Physics*, *121*, 3439–3451. https://doi.org/10.1002/2015JA021895

Bust, G. S., & Crowley, G. (2007). Tracking of polar cap ionospheric patches using data assimilation. *Journal of Geophysical Research*, *112*, A05307. https://doi.org/10.1029/2005JA011597

Bust, G. S., & Mitchell, C. N. (2008). History, current state, and future directions of ionospheric imaging. *Reviews of Geophysics*, *46*, RG1003. https://doi.org/10.1029/2006RG000212

Carlson, H. C. (2012). Sharpening our thinking about polar cap ionospheric patch morphology, research, and mitigation techniques. *Radio Science*, *47*, RS0L21. https://doi.org/10.1029/2011RS004946

Carlson, H. C., Moen, J., Oksavik, K., Nielsen, C. P., McCrea, I. W., Pedersen, T. R., & Gallop, P. (2006). Direct observations of injection events of subauroral plasma into the polar cap. *Geophysical Research Letters*, *33*, L05103. https://doi.org/10.1029/2005GL025230

Chartier, A., Mitchell, N. C., & Jackson, D. (2012). A 12 year comparison of MIDAS and IRI 2007 ionospheric total electron content. *Advances in Space Research*, *49*, 1348–1355.

Chisham, G., Lester, M., Milan, S. E., Freeman, M. P., Bristow, W. A., Grocott, A., et al. (2007). A decade of the Super Dual Auroral Radar Network (SuperDARN): Scientific achievements, new techniques and future directions. *Surveys in Geophysics*, *28*(1), 33–109. https://doi.org/10.1007/s10712-007-9017-8

Cousins, E. D. P., & Shepherd, S. G. (2010). A dynamical model of high-latitude convection derived from SuperDARN plasma drift measurements. *Journal of Geophysical Research*, *115*, A12329. https://doi.org/10.1029/2010JA016017

Crowley, G. (1996). *Critical review of ionospheric patches and blobs* (pp. 619–648). New York: University Press.

du Toit, P. C., & Marsden, J. E. (2010). Horseshoes in hurricanes. *Journal of Fixed Point Theory and Applications*, *7*(2), 351–384. https://doi.org/10.1007/s11784-010-0028-6

Gjerloev, J. W., Waters, C. L., & Barnes, R. J. (2018). Deriving global convection maps from SuperDARN measurements. *Journal of Geophysical Research: Space Physics*, *123*, 2902–2915. https://doi.org/10.1002/2017JA024543

Greenspan, M. E., Anderson, P. B., & Pelagatti, J. M. (1986). Characteristics of the thermal plasma monitor (SSIES) (Special sensor for ions, electrons, and scintillation) for the defense meteorological satellite program (DMSP) spacecraft S8 through S10, 117.

Haller, G. (2015). Lagrangian coherent structures. *Annual Review of Fluid Mechanics*, *47*(1), 137–162. https://doi.org/10.1146/annurev-fluid-010313-141322

Hardy, D. A., Schmitt, L. K., Gussenhoven, M. S., Marshall, F. J., & Yeh, H. C. (1984). Precipitating electron and ion detectors (SSJ/4) for the block 5D/flights 6-10 DMSP (defense meteorological satellite program) satellites: Calibration and data presentation.

Hunsucker, R. D., & Hargreaves, J. K. (2003). *The high-latitude ionosphere and its effects on radio propagation*. Cambridge, UK: Cambridge University Press.

Khazanov, G. V. (2016). *Space weather fundamentals* (1st ed.). Boca Raton, FL: CRC Press.

King, J. H., & Papitashvili, N. E. (2005). Solar wind spatial scales in and comparisons of hourly Wind and ACE plasma and magnetic field data. *Journal of Geophysical Research*, *110*, A02104. https://doi.org/10.1029/2004JA010649

Kirchengast, G. (1996). The Graz ionospheric flux tube simulation model, (R. W. Schunk)., *Solar-terrestrial energy program: Handbook of ionospheric models* (pp. 73–94). Logan, UT: Center for Atmospheric and Space Sciences.

Lockwood, M., & Carlson, H. C. (1992). Production of polar cap electron density patches by transient magnetopause reconnection. *Geophysical Research Letters*, *19*(17), 1731–1734. https://doi.org/10.1029/92GL01993

Lockwood, M., McCrea, I. W., Milan, S. E., Moen, J., Cerisier, J. C., & Thorolfsson, A. (2000). Plasma structure within poleward-moving cusp/cleft auroral transients: Eiscat svalbard radar observations and an explanation in terms of large local time extent of events. *Annales Geophysicae*, *18*(9), 1027–1042. https://doi.org/10.1007/s00585-000-1027-5

Mitchell, C. N., & Spencer, P. S. J. (2003). A three-dimensional time-dependent algorithm for ionospheric imaging using GPS. *Annals of Geophysics*, *46*(4), 687–696. https://doi.org/10.4401/ag-4373

Moen, J., Carlson, H. C., Oksavik, K., Nielsen, C. P., Pryse, S. E., Middleton, H. R., et al. (2006). Eiscat observations of plasma patches at sub-auroral cusp latitudes. *Annales Geophysicae*, *24*(9), 2363–2374. https://doi.org/10.5194/angeo-24-2363-2006

Moen, J., Oksavik, K., Alfonsi, L., Daabakk, Y., Romano, V., & Spogli, L. (2013). Space weather challenges of the polar cap ionosphere. *Journal of Space Weather and Space Climate*, *3*, A02. https://doi.org/10.1051/swsc/2013025

Peacock, T., & Haller, G. (2013). Lagrangian coherent structures: The hidden skeleton of fluid flows. *Physics Today*, *66*(2), 41. https://doi.org/10.1063/PT.3.1886

Pi, X., Iijima, B. A., & Lu, W. (2017). Effects of ionospheric scintillation on GNSS-based positioning. *Navigation*, *64*(1), 3–22. https://doi.org/10.1002/navi.182

Pikovsky, P. A., & Politi, A. (2016). *Lyapunov exponents: A tool to explore complex dynamics*. Cambridge: Cambridge University Press. https://doi.org/10.1017/CBO9781139343473

Rodger, A. S., Pinnock, M., Dudeney, J. R., Baker, K. B., & Greenwald, R. A. (1994). A new mechanism for polar patch formation. *Journal of Geophysical Research*, *99*(A4), 6425–6436. https://doi.org/10.1029/93JA01501

Ruohoniemi, J. M., & Baker, K. B. (1998). Large-scale imaging of high-latitude convection with Super Dual Auroral Radar Network HF radar observations. *Journal of Geophysical Research*, *103*(A9), 20,797–20,811. https://doi.org/10.1029/98JA01288

Ruohoniemi, J. M., & Greenwald, R. A. (1996). Statistical patterns of high-latitude convection obtained from Goose Bay HF radar observations. *Journal of Geophysical Research*, *101*(A10), 21,743–21,763. https://doi.org/10.1029/96JA01584

Ruohoniemi, J. M., & Greenwald, R. A. (2005). Dependencies of high-latitude plasma convection: Consideration of interplanetary magnetic field, seasonal, and universal time factors in statistical patterns. *Journal of Geophysical Research*, *110*, A09204. https://doi.org/10.1029/2004JA010815

Shadden, S. C., Lekien, F., & Marsden, J. E. (2005). Definition and properties of Lagrangian coherent structures from finite-time Lyapunov exponents in two-dimensional aperiodic flows. *Physica D: Nonlinear Phenomena*, *212*(3), 271–304. https://doi.org/10.1016/j.physd.2005.10.007

Shepherd, S. G., & Ruohoniemi, J. M. (2000). Electrostatic potential patterns in the high-latitude ionosphere constrained by SuperDARN measurements. *Journal of Geophysical Research*, *105*(A10), 23,005–23,014. https://doi.org/10.1029/2000JA000171

Sotnikov, V., Kim, T., Lundberg, J., Paraschiv, I., & Mehlhorn, T. A. (2014). Scattering of electromagnetic waves by vortex density structures associated with interchange instability: Analytical and large scale plasma simulation results. *Physics of Plasmas*, *21*(5), 052309. https://doi.org/10.1063/1.4879021

Spencer, P., & Mitchell, C. (2007). Imaging of fast moving electron-density structures in the polar cap. *Annals of Geophysics*, *50*(3), 427–434. https://doi.org/10.4401/ag-3074

Tascione, T. F. (2012). *Introduction to the space environment, Orbit: A Foundation Series* (2nd ed.). Malabar, FL: Krieger Publishing Company.

Thébault, E., Finlay, C. C., Beggan, C. D., Alken, P., Aubert, J., Barrois, O., et al. (2015). International geomagnetic reference field: The 12th generation. *Earth, Planets and Space*, *67*(1), 79. https://doi.org/10.1186/s40623-015-0228-9

Venditti, J. G., Hardy, R. J., Church, M., & Best, J. L. (2013). What is a coherent flow structure in geophysical flow? *Coherent flow structures at earth's surface* (pp. 1–16). Chichester, UK: John Wiley. https://doi.org/10.1002/9781118527221.ch1

Wang, N. (2018). Lagrangian coherent structures in the ionosphere-thermosphere system (PhD thesis).

Wang, N., Datta-Barua, S., Chartier, A., Ramirez, U., & Mitchell, C. N. (2018). Horseshoes in the high-latitude ionosphere. *Journal of Geophysical Research: Space Physics*, *123*, 5831–5849. https://doi.org/10.1029/2017JA025077

Wang, N., Ramirez, U., Flores, F., & Datta-Barua, S. (2017). Lagrangian coherent structures in the thermosphere: Predictive transport barriers. *Geophysical Research Letters*, *44*, 4549–4557. https://doi.org/10.1002/2017GL072568

Weimer, D. R. (2005). Predicting surface geomagnetic variations using ionospheric electrodynamic models. *Journal of Geophysical Research*, *110*, A12307. https://doi.org/10.1029/2005JA011270

Yeh, K. C., & Liu, C.-H. (1982). Radio wave scintillations in the ionosphere. Proc. IEEE, *70*(4), 324–360. https://doi.org.10.1109/PROC.1982.12313

Zhang, Q.-H., Lockwood, M., Foster, J. C., Zhang, S.-R., Zhang, B.-C., McCrea, I. W., et al. (2015). Direct observations of the full Dungey convection cycle in the polar ionosphere for southward interplanetary magnetic field conditions. *Journal of Geophysical Research: Space Physics*, *120*, 4519–4530. https://doi.org/10.1002/2015JA021172

Zhang, Q.-H., Moen, J., Lockwood, M., McCrea, I., Zhang, B.-C., McWilliams, K. A., et al. (2016). Polar cap patch transportation beyond the classic scenario. *Journal of Geophysical Research: Space Physics*, *121*, 9063–9074. https://doi.org/10.1002/2016JA022443

Zhang, Q.-H., Zhang, B.-C., Liu, R.-Y., Dunlop, M. W., Lockwood, M., Moen, J., et al. (2011). On the importance of interplanetary magnetic field |*By*| on polar cap patch formation. *Journal of Geophysical Research*, *116*, A05308. https://doi.org/10.1029/2010JA016287

Zhang, Q.-H., Zhang, B.-C., Lockwood, M., Hu, H.-Q., Moen, J., Ruohoniemi, J. M., et al. (2013). Direct observations of the evolution of polar cap ionization patches. *Science*, *339*(6127), 1597–1600. https://doi.org/10.1126/science.1231487

Zhang, Q.-H., Zhang, B.-C., Moen, J., Lockwood, M., McCrea, I. W., Yang, H.-G., et al. (2013). Polar cap patch segmentation of the tongue of ionization in the morning convection cell. *Geophysical Research Letters*, *40*, 2918–2922. https://doi.org/10.1002/grl.50616